UNIVERSITY OF COPENHAGEN

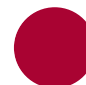

Primary thermometry of a single reservoir using cyclic electron tunneling to a quantum dot

Ahmed, Imtiaz; Chatterjee, Anasua; Barraud, Sylvain; Morton, John J. L.; Haigh, James A.; Gonzalez-Zalba, M. Fernando

Published in:
Communications Physics

DOI:
10.1038/s42005-018-0066-8

Publication date:
2018

Document version
Publisher's PDF, also known as Version of record

Document license:
CC BY

Citation for published version (APA):
Ahmed, I., Chatterjee, A., Barraud, S., Morton, J. J. L., Haigh, J. A., & Gonzalez-Zalba, M. F. (2018). Primary thermometry of a single reservoir using cyclic electron tunneling to a quantum dot. *Communications Physics*, *1*, [66]. https://doi.org/10.1038/s42005-018-0066-8

Download date: 26. okt.. 2020

COMMUNICATIONS PHYSICS

ARTICLE

DOI: 10.1038/s42005-018-0066-8 OPEN

Primary thermometry of a single reservoir using cyclic electron tunneling to a quantum dot

Imtiaz Ahmed[1], Anasua Chatterjee[2,3], Sylvain Barraud[4], John J.L. Morton[2,5], James A. Haigh[6] & M. Fernando Gonzalez-Zalba[6]

At the nanoscale, local and accurate measurements of temperature are of particular relevance when testing quantum thermodynamical concepts or investigating novel thermal nanoelectronic devices. Here, we present a primary electron thermometer that allows probing the local temperature of a single-electron reservoir in single-electron devices. The thermometer is based on cyclic electron tunneling between a system with discrete energy levels and the reservoir. When driven at a finite rate, close to a charge degeneracy point, the system behaves like a variable capacitor whose full width at half maximum depends linearly with temperature. We demonstrate this type of thermometer using a quantum dot in a silicon nanowire transistor. We drive cyclic electron tunneling by embedding the device in a radio-frequency resonator which in turn allows reading the thermometer dispersively. Overall, the thermometer shows potential for local probing of fast heat dynamics in nanoelectronic devices and for seamless integration with silicon-based quantum circuits.

[1] Cavendish Laboratory, University of Cambridge, J. J. Thomson Avenue, Cambridge CB3 0HE, UK. [2] London Centre for Nanotechnology, University College London, London WC1H 0AH, UK. [3] Center for Quantum Devices, Niels Bohr Institute, University of Copenhagen, 2100 Copenhagen, Denmark. [4] CEA/LETI-MINATEC, CEA-Grenoble, 38000 Grenoble, France. [5] Department of Electronic & Electrical Engineering, University College London, London WC1E 7JE, UK. [6] Hitachi Cambridge Laboratory, J. J. Thomson Avenue, Cambridge CB3 0HE, UK. Correspondence and requests for materials should be addressed to I.A. (email: ia307@cam.ac.uk) or to M.F.G.-Z. (email: mg507@cam.ac.uk)

An essential element in low temperature experimental physics is the thermometer[1]. Sensors that link temperature to another physical quantity in an accurate, fast, stable, and compact manner are desired. If the link is done via a well-known physical law, the sensor is called a primary thermometer because it removes the need of calibration to a second thermometer.

Several primary thermometers have been developed for low temperature applications. A common technique is based on the Johnson-Nyquist noise of a resistor[2] which can be used in combination with superconducting quantum interference devices to perform current-sensing noise thermometry (CSNT)[3]. Shot-noise thermometry (SNT)[4–6] uses the temperature-dependent voltage scaling of the noise power of a biased tunnel junction. Coulomb blockade thermometry (CBT) makes use of charging effects in two-terminal devices with multiple tunnel junctions[7–9]. Thermometry using counting statistics via single-electron devices is also possible[10–14]. However, in all these cases, the sensors require a continuous flow of electrons from source to drain in two terminal devices which, for particular experiments such as in single-molecule junction and single-nanoparticle devices, might not be possible or even desirable[15,16].

Moreover, recent advances in device nanoengineering have led to a focused interest in using concepts from quantum thermodynamics[17–21] to improve the efficiency of technologies such as the thermal diode[22,23] or thermal energy harvesters[24]. In these nanoelectronic devices, determining the local temperature in different reservoirs of the device is of particular relevance but challenging from an experimental perspective.

Here, we demonstrate a type of primary thermometer that uses cyclic electron tunneling to measure the temperature of a single electron reservoir without the need of electrical transport. The tunneling occurs between a system with a zero-dimensional (0D) density of states (DOS) -in this case a quantum dot (QD)—and a single electron reservoir of unknown temperature. Our thermometer relates temperature and capacitance changes with a well known physical law by using the ratio k_B/e between the Boltzmann constant and the electron charge. The thermometer is driven and read out by an electrical resonator at radio-frequencies. In this proof-of-principle experiment, we perform primary thermometry down to 1 K but show that the operational temperature range of the sensor can be extended in-situ using electrostatic fields. Our experimental results follow our theoretical predictions of the temperature-dependent capacitance of the system. The thermometer is implemented in a complementary-metal-oxide-semiconductor (CMOS) transistor which makes it suitable for large-scale manufacturing and seamless integration with silicon-based quantum circuits, a promising platform for the implementation of a scalable quantum computer[25–27].

Results

Theory. We consider a QD in thermal equilibrium with an electron bath whose temperature T we wish to measure. The QD is capacitively coupled to a gate electrode C_{tg}, and tunnel coupled to the reservoir via a tunnel junction with capacitance C_j and resistance R_j, see Fig. 1a. The system is operated in the quantum confinement regime such that electrons occupy discrete energy levels of the QD. The coupled QD-reservoir system has an associated differential capacitance[28,29] C_{diff} as seen from the gate given by

$$C_{diff} = \frac{\partial Q}{\partial V_{tg}} = \underbrace{\alpha C_j}_{\text{geometrical}} \underbrace{- e\alpha \frac{\partial P_1}{\partial V_{tg}}}_{\text{tunneling}}, \qquad (1)$$

where Q is the net charge in the QD, V_{tg} is the gate voltage, e is the electron charge, α is the gate coupling $C_{tg}/(C_j + C_{tg})$, and P_1 is the probability of having an excess electron in the QD. The first term in Eq. (1) represents the DC limit of the capacitance, the geometrical capacitance, whereas the second term represents the parametric dependence of the excess electron probability on gate voltage, the tunneling capacitance. The second term is the focus of this Article.

To obtain an analytical expression for the tunneling capacitance C_t, we next consider the QD-reservoir charge distribution in detail. In the limit of weak tunnel coupling, the QD-reservoir system can be described by the Hamiltonian $H = \frac{1}{2}\varepsilon\sigma_z$ where ε is the energy detuning and σ_z is the z Pauli matrix. The eigenenergies $E_0 = \varepsilon/2$ and $E_1 = -\varepsilon/2$ are associated with the QD states with zero and one excess electron, respectively. This additional electron can tunnel in and out of the electron reservoir at a rate γ, as schematically depicted in Fig. 1b. The energy detuning between these states can be controlled by V_{tg} given that $\varepsilon = -e\alpha(V_{tg} - V_0)$. Here V_0 is the gate voltage offset at which the two eigenstates are degenerate.

To probe the tunneling capacitance, the system is subject to a modulation occurring at some frequency, f_r that varies the energy detuning $\varepsilon = \varepsilon_0 + \delta\varepsilon \sin(2\pi f_r t)$. In the limit $\gamma \gg f_r$, the QD and reservoir are in thermal equilibrium and electrons tunnel in and out of the reservoir adiabatically. In this situation, P_1 tracks the thermal population, P_1^0, given by the instantaneous gate-voltage excitation[28] and C_t can be expressed as

$$C_t = -e\alpha \frac{\partial P_1^0}{\partial V_{tg}} = (e\alpha)^2 \frac{\partial P_1^0}{\partial \varepsilon}. \qquad (2)$$

From the energy spectrum represented in Fig. 1c and taking into account the spin degeneracy of two in the QD, Maxwell–Boltzmann statistics give the equilibrium probability distribution

$$P_1^0 = \frac{2\exp(\varepsilon/2k_BT)}{\exp(-\varepsilon/2k_BT) + 2\exp(\varepsilon/2k_BT)}, \qquad (3)$$

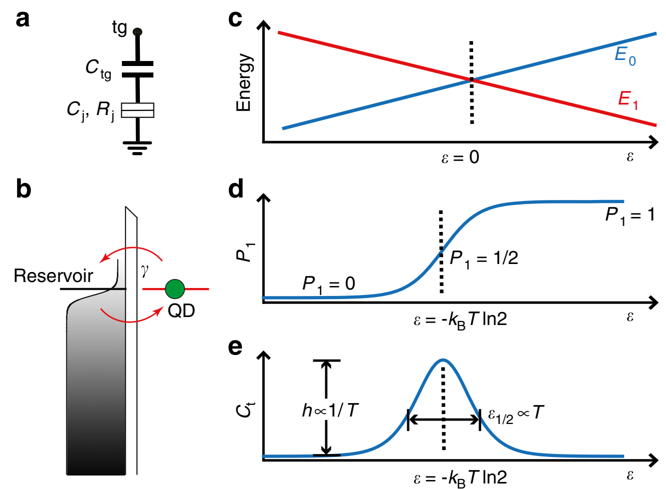

Fig. 1 Theory. **a** Circuit equivalent of the quantum dot (QD)-reservoir system. **b** Schematic of cyclic electron exchange between a discrete energy level of a QD and a thermally broadened electron reservoir. **c** Energy diagram of a fast driven two-level-system (TLS) with discrete energies E_0 and E_1, across a charge degeneracy point. **d** Probability P_1 of an electron to be in the QD as a function of energy level detuning ε. **e** Tunneling capacitance C_t as a function of ε

and this is depicted as a function of detuning in Fig. 1d. At large negative detuning the QD remains unoccupied $\left(P_1^0 = 0\right)$, at large positive detuning the QD is occupied $\left(P_1^0 = 1\right)$, and at $\varepsilon = -k_\mathrm{B}T\ln 2, P_1^0 = 1/2$. We calculate the tunneling capacitance of the system and obtain

$$C_\mathrm{t} = \frac{(e\alpha)^2}{4k_\mathrm{B}T}\frac{1}{\cosh^2\left(\frac{\varepsilon}{2k_\mathrm{B}T}\right)}. \quad (4)$$

where we have redefined the detuning ε to account for the peak-center shift induced by temperature ($\varepsilon \to \varepsilon + k_\mathrm{B}T\ln 2$). Thus the tunneling capacitance C_t has a full width at half maximum (FWHM) with respect to ε of

$$\varepsilon_{1/2} = 4\ln\left(\sqrt{2}+1\right)k_\mathrm{B}T, \quad (5)$$

as plotted in Fig. 1e. Since $\varepsilon_{1/2} = e\alpha V_{1/2}$, the analysis shows it is possible to obtain the temperature of the electron reservoir from the FWHM of the C_t vs V_tg curve once the gate lever arm α is known. The quantity $V_{1/2}$ is the FWHM with respect to gate voltage. Furthermore, from Eq. (4) we see that the peak amplitude C_t^0 of the tunneling capacitance C_t, is inversely proportional to the reservoir temperature T,

$$C_\mathrm{t}^0 \propto \frac{1}{T}. \quad (6)$$

In the case of a finite magnetic field (see Supplementary Note 1), the expressions for $\varepsilon_{1/2}$ and C_t^0 remain as in Eqs. (5) and (6), respectively. We note that the C_t peak center shifts to lower detuning values as the magnetic field B is increased, see Supplementary Fig. 1a, b. The shift tends to $\varepsilon(B) = \varepsilon(0) - g\mu_\mathrm{B}|B|/2$ for $g\mu_\mathrm{B}|B| > k_\mathrm{B}T$, where g is the electron g-factor and μ_B is the Bohr magneton. This demonstrates our proposed method of determining the reservoir temperature T from capacitance C_t measurements is independent of magnetic field. We note that our analysis is valid as long as $k_\mathrm{B}T$ remains smaller than the discrete energy spacing in the QD (ΔE) and larger than the QD level broadening ($h\gamma$). These two conditions set the temperature range in which thermometry by cyclic electron tunneling is accurate. In the latter case ($k_\mathrm{B}T < h\gamma$), C_t takes a Lorentzian form given by

$$C_\mathrm{t} = \frac{(\alpha e)^2}{\pi}\frac{h\gamma}{(h\gamma)^2 + \varepsilon^2}. \quad (7)$$

and $\varepsilon_{1/2}$ is given by $2h\gamma$[30], and is thus no longer temperature dependent. The relaxation rate γ is directly linked to the shape of the tunnel barrier between the QD and the reservoir which can be tuned electrically by, for example, a gate electrode. The tunneling capacitance C_t can be probed with high-frequency techniques such as gate-based reflectometry[31,32] and can be used to measure temperature. We refer to this sensor as the gate-based electron thermometer (GET).

Device and high-frequency resonator. The device used here is a silicon nanowire field-effect transistor (NWFET)[33] fabricated in fully-depleted silicon-on-insulator (SOI) following CMOS fabrication processes. At low temperatures, gate-defined QDs form in the channel of the NWFET[34,35], see Fig. 2a. The transistor has a channel length $l = 44$ nm and width $w = 42$ nm. The 8 nm thick NW channel was pattered on SOI above the 145 nm buried oxide (BOX). The gate oxide consists of 0.8 nm SiO_2 and 1.9 nm HfSiON resulting in an equivalent gate oxide thickness of 1.3 nm. The top-gate (tg) is formed using 5 nm TiN and 50 nm poly-crystalline silicon. The NW channel is separated from the highly doped source and drain reservoirs by 20 nm long Si_3N_4 spacers. The silicon wafer under the BOX can be used as a global back-gate (bg).

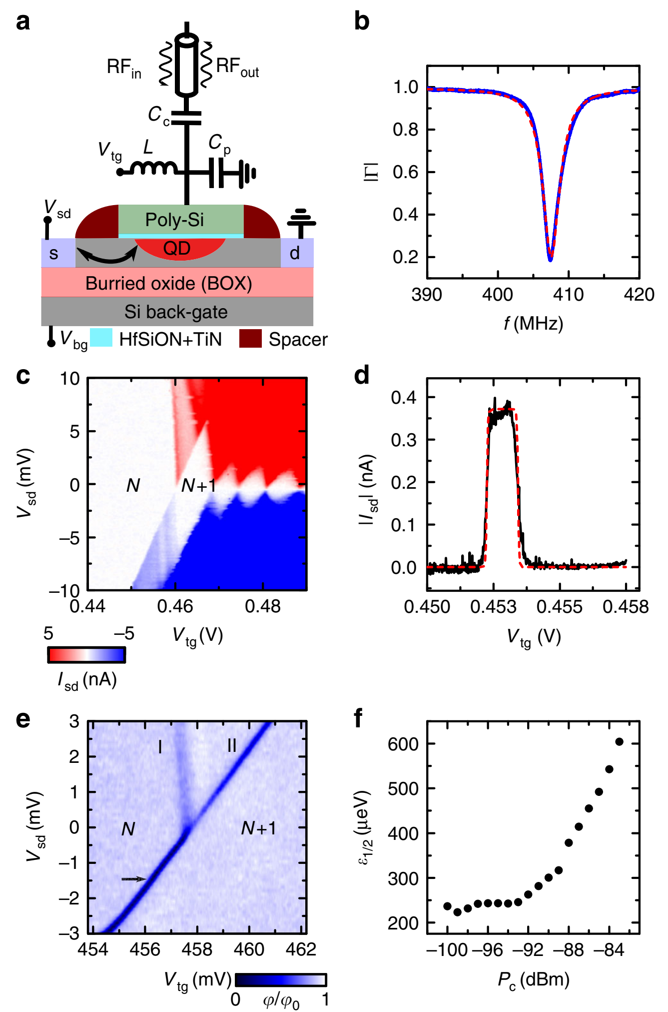

Fig. 2 Setup and calibration. **a** Schematic of the device along the nanowire (NW) showing the source (s), drain (d), top-gate (tg) and back-gate (bg) terminals. The LC resonator is formed with a surface mount inductor L connected to the top-gate and the parasitic capacitance to ground C_p. C_c decouples the resonator from the line. V_sd, V_tg, and V_bg are source, top-gate and back-gate bias voltages. **b** The amplitude $|\Gamma|$ of the reflection coefficient as function of frequency f: data in blue and a Lorentzian fit in red. **c** Source to drain current I_sd as a function of V_sd and V_tg showing Coulomb diamonds. **d** I_sd trace as a function of V_tg at $V_\mathrm{sd} = -1.5$ mV: data in black and fit in red. **e** Relative demodulated phase ϕ/ϕ_0 as a function of V_sd and V_tg showing the stability map of the first electronic transition. The symbol I(II) indicates the electronic transition from source(drain) to quantum dot. N and $N+1$ indicate the bias regions with fixed electron number. The arrow indicates the bias region for thermometry. **f** The full width at half maximum (FWHM) $\varepsilon_{1/2}$ of the charge transition line II as function of rf-carrier power P_c. The error bars are smaller than the size of the dots. The error includes the uncertainties in the gate lever arm α and the full width at half maximum measurements

To probe the device tunneling capacitance, we embed the transistor in a resonator formed by a 470 nH inductor—connected to the top-gate (tg) of the device—and the device parasitic capacitance C_p, which appears in parallel with the differential capacitance of the device, as can be seen in Fig. 2a. We couple the resonator to a high-frequency line via a coupling capacitor $C_\mathrm{c} = 130$ fF. In order to characterize the resonator, we

measure the reflection coefficient Γ. In Fig. 2b, we plot the magnitude |Γ| (data in blue and a fit in red) as a function of frequency f at a fixed back-gate voltage $V_{bg} = 3$ V. We extract the resonator's natural frequency of oscillation, $f_0 = 1/\left(2\pi\sqrt{L\left(C_c + C_p\right)}\right) = 408$ MHz, the bandwidth BW = 2.9 MHz, the loaded quality factor $Q_L = 141$ and $C_p = 194$ fF. We find that the resonator is overcoupled but the depth of resonance, $|\Gamma|_{min} = 0.18$ indicates that the resonator is close to being matched to the line.

The nature of cyclic electron tunneling. A system with discrete energy levels E_0 and E_1 as described in the Sec. Theory, can be found in a 0D QDs where the DOS consists of a series of delta functions at discrete energies[36]. In this section, we demonstrate the discrete nature of the QD in NWFET using electrical transport measurements.

We measure the source-drain current I_{sd} as function of V_{tg} and source-drain voltage V_{sd}. The source-drain current I_{sd} shows characteristic Coulomb blockade diamonds when measured as a function of V_{tg} and V_{sd}, see Fig. 2c. Coulomb blockade diamonds are a signature of sequential single-electron transport through the QD from the source (s) to drain (d) reservoir. From the height of the Coulomb diamond in the charge stable configuration, we extract the QD first addition energy, $E_{add} = 6$ meV, and 3.75 meV for subsequent additions. Such a variable E_{add} is characteristic of the few-electron regime where transport occurs through single-particle (0D) energy levels.

When the QD has a 0D DOS and the source(drain) reservoirs have a 3D DOS, then Fermi's golden rule yields for the source (drain) tunnel rate

$$\gamma_{s(d)} = \frac{\gamma_{0,s(d)}}{1 + \exp\left(-\varepsilon_{s(d)}/k_B T\right)}, \quad (8)$$

where $\varepsilon_{s(d)}$ is the level detuning between the QD and s(d) reservoirs and $\gamma_{0,s(d)}$ is the tunnel rate at $\varepsilon_{s(d)} = 0$[32]. Note that these tunnel rates are significantly different from metallic (3D DOS) QDs tunnel coupled to 3D reservoirs[37]. Assuming that a single discrete energy level of the QD is within the energy window eV_{sd}, the source drain current I_{sd} can be written in terms of tunneling rates γ_s and γ_d by the relation $I_{sd} = e\gamma_s\gamma_d/(\gamma_s + \gamma_d)$[38] and is fitted to the data measured at fixed $V_{sd} = -1.5$ mV in Fig. 2d. The agreement between the data and the fit demonstrates the 0D nature of the QD, showing it is suitable for the electron thermometry method introduced in the Sec. Theory. Moreover, the top hat shape shows that there are no excited states within 1.5 meV of the ground state. Excited states at an energy comparable or lower than $2 \times 3.53 k_B T$ could interfere with the method but the fit reveals they could only become an issue at temperatures $T \geq 2.5$ K.

Gate coupling and optimal power. In order to get an accurate reading of the temperature T from Eq. (5), the gate lever arm α needs to be obtained. We use gate-based reflectometry techniques to probe the charge stability map of the QD in the voltage region of interest, see Fig. 2e taken at 50 mK. We excite the resonator at resonant frequency f_0 and monitor the reflected signal. We used standard homodyne detection techniques[32] to measure the demodulated phase response φ of the resonator as a function of V_{sd} and V_{tg}. The phase of the resonators changes (dark blue lines I and II in Fig. 2e) at the charge degeneracy points due to a tunneling capacitance contribution. The separation in V_{tg} between I and II, ΔV_{tg}, at a given V_{sd} gives a measurement of $\alpha = V_{sd}/\Delta V_{tg}$. We repeat these measurements for several V_{sd} and obtain ΔV_{tg} as a function of V_{sd}, providing a measure of α from the slope and of the V_{sd} offset from the intercept. We obtain $\alpha = 0.9 \pm 0.01$, and this large value —close to 1— is consistent with the multi-gate geometry and the small equivalent gate oxide thickness of 1.3 nm of NWFETs[32]. We consider α temperature-independent[6,39], because the capacitances that define α are determined by the geometry of the device and the voltage bias applied to the electrodes which we keep constant throughout the range of temperatures measured.

Finally, we calibrate the optimal power on the resonator using transition II at $V_{sd} = -1.5$ mV, which we will subsequently use to perform thermometry. In Fig. 2f, we plot $\varepsilon_{1/2}$ as a function of the carrier power P_c at the input of the resonator. At high carrier power, $P_c > -93$ dBm, $\varepsilon_{1/2}$ increases with P_c indicating the transition is power broadened. For $P_c < -93$ dBm, $\varepsilon_{1/2}$ remains independent of P_c and hence, we observe the intrinsic linewidth of the transition. We select $P_c = -95$ dBm hereinafter.

Primary thermometry. In this section, we explore experimentally gate-based primary thermometry using transition II (see Fig. 2e). As we have seen in the Sec. Theory, when $k_B T/h > \gamma > f_0$, electron tunneling between QD and reservoir has an associated tunneling capacitance whose $\varepsilon_{1/2}$ gives a reading of the reservoir temperature (see Eq. (5)). In this experiment, we probe T from a measurement of φ vs ε, since $\varphi = -2Q_L C_t/C_p$[40–42], when the resonator is overcoupled to the line. We drive the resonator at frequency f_0 and monitor φ as we sweep ε across the charge degeneracy for different temperatures of the mixing chamber T_{mc}, see Fig. 3a. We measure T_{mc} with a 2200 Ω RuO_2 resistive thermometer. As the temperature is increased, $\varepsilon_{1/2}$ increases and the maximum phase shift decreases. We fit the data to Eq. (4) (red dotted lines), extract $\varepsilon_{1/2}$ for several T_{mc} and plot it Fig. 3b (black dots). Two clear temperature regimes become apparent:

At low temperatures, for $T_{mc} < 200$ mK, we see that $\varepsilon_{1/2}$ is independent of T_{mc} and equal to 160 μeV (blue dotted line). In this regime, as we shall demonstrate later, the thermal energy is smaller than the QD level broadening ($k_B T < h\gamma$). As a result, the temperature reading of the GET, T_{GET}, deviates from the mixing chamber thermometer. On the other hand, at high temperatures, $T_{mc} > 1$ K, we observe that $\varepsilon_{1/2}$ presents a linear dependence with T_{mc} as predicted by Eq. (5). For comparison, we plot the theoretical prediction (red dashed line) and observe that both follow a similar trend. In this regime, since $h\gamma < k_B T$, the GET can be used to obtain an accurate reading of the temperature of the electron reservoir. We quantify the precision of the thermometer by measuring the fractional uncertainty in the temperature reading of the gate-based thermometer, $\delta T_{GET}/T_{GET}$ (see Fig. 3c). At low temperatures, the precision of the thermometer is primarily determined by the uncertainty in the lever arm, $\delta\alpha/\alpha = 1.1\%$. As we raise the temperature, the phase response of the resonator becomes smaller leading to an increase in the uncertainty of $V_{1/2}$ which, at the highest temperatures, becomes comparable to that of α. We find $\delta T_{GET}/T_{GET}$ increases up to 1.6%. Additionally, in Fig. 3d, we determine the fractional accuracy of the GET thermometer, $\Delta T/T_{mc}$ by comparing its reading with that of the RuO_2 thermometer ($\Delta T = T_{GET} - T_{mc}$). We see than the discrepancy between thermometers is less than 8% for temperatures higher than 1 K and this goes down to an average of 3.5% above 1.5 K. The error in the accuracy is primarily determined by the uncertainty in the reading of the RuO_2 thermometer, which varies from 1% at the lowest temperatures to 6% at 2.4 K, rather than by the precision of the GET.

We note that, although not applicable for primary thermometry purposes, the whole temperature range can be described by a single expression that combines both regimes, level-broadening

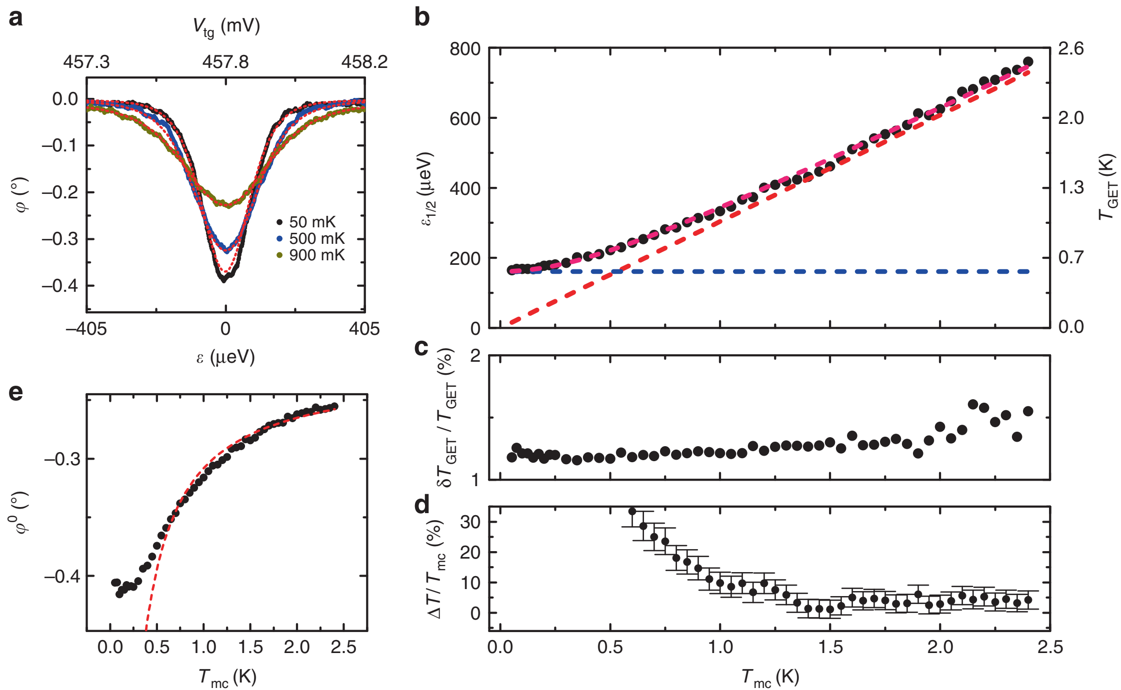

Fig. 3 Primary thermometry. **a** Phase response φ of the resonator as a function of top-gate voltage V_{tg} swept across a charge degeneracy point for different T_{mc}. The red dotted lines are fits using Eq. (4). **b** $\varepsilon_{1/2}$ and T_{GET} as a function of mixing chamber temperature T_{mc} (black dots). Theoretical predictions to the low temperature regime (dashed blue), high temperature regime (dashed red) and full temperature range (dashed magenta). **c** Fractional temperature precision $\delta T_{GET}/T_{GET}$ and **d** fractional accuracy $\Delta T/T_{mc}$ as a function of T_{mc}. $\Delta T = T_{GET} - T_{mc}$. The error includes the uncertainties in T_{mc} and T_{GET} measurements. **e** Phase change at φ^0 as a function T_{mc} (black dots) and a $1/T_{mc}$ fit at high temperature $T_{mc} > 1$ K (red dashed line)

and thermal broadening, in to a single expression $\varepsilon_{1/2} = \sqrt{(3.53k_BT)^2 + (2h\gamma)^2}$ (see magenta dashed line in Fig. 3b). This formula fits well the data and we find that the difference is <6% for all temperatures.

Lastly, in Fig. 3e, we plot the maximum phase shift φ^0 extracted from the fit, as a function of T_{mc}. Again, the two regimes are apparent. At low temperatures φ^0 remains constant and only at temperatures $T_{mc} > 1$ K, φ^0 shows an inverse proportionality with T_{mc} as predicted by Eq. (6) (dashed red line).

Low temperature limit. In Fig. 3b, e, we have seen that at low temperatures both $\varepsilon_{1/2}$ and φ^0 deviate from the prediction in Sec. Theory. In this regime, the gate-sensor cannot be used as an accurate thermometer. Two mechanisms may be responsible for this discrepancy: Electron-phonon decoupling, due to the weaker interaction at low T[8,10], or lifetime broadening, when the QD energy levels are broadened beyond the thermal broadening of the reservoir, which occurs when $h\gamma > k_BT$. In the latter case, $\varepsilon_{1/2}$ is given by $2h\gamma$ (see Eq. (7)) whereas for the former, it is given by $3.53k_BT_{dec}$, where T_{dec} is the decoupling temperature.

To assess the origin of the discrepancy, we modify the tunnel barrier potential by varying the vertical electric field across the device (Fig. 4a) which effectively changes γ[32]. We do so by changing the potential on the back-gate electrode V_{bg} while compensating with V_{tg}. In Fig. 4b, we plot $\varepsilon_{1/2}$ as a function of V_{bg}. We see that as we lower V_{bg}, $\varepsilon_{1/2}$ decreases, indicating that the tunnel rate γ across the potential barrier is lower due to the increasing height of the potential barrier at lower V_{bg}. This trend indicates that at low temperature, our primary thermometer is limited by level broadening and not by electron–phonon decoupling. Moreover, it demonstrates it is possible to tune electrically the low temperature range of the primary thermometer, as long as γ remains larger than the excitation frequency f_0.

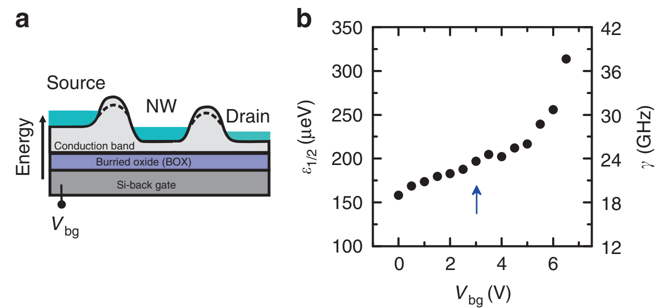

Fig. 4 Low temperature limit. **a** Schematic of the conduction band edge along the nanowire channel. The quantum dot-reservoir tunnel barriers can be controlled "in-situ". **b** The full width at half maximum $\varepsilon_{1/2}$ and the tunnel rate γ as a function of back-gate voltage V_{bg}. The arrow indicates the V_{bg} at which thermometry was performed. The error bars are smaller than the size of the dots. The error includes the uncertainties in the gate lever arm α and the $\varepsilon_{1/2}$ measurements

Discussion

We have described and demonstrated a novel primary electron thermometer based on cyclic electron tunneling that allows measuring the temperature of a single electron reservoir without the need of electrical transport. The GET requires of a system with discrete energy levels tunnel-coupled to the reservoir to be measured, a scenario that can be found in a broad range of nanolectronics devices such as single-molecule junctions and/or in single-electron devices. Here, we have implemented the thermometer with a QD using CMOS technology which makes it ideal for large-scale production. Driving and readout of the thermometer can be performed simultaneously using reflectometry techniques which have recently demonstrated high-sensitivity with MHz bandwidth[43]. Since the driving must be

done in the adiabatic limit, the GET is likely to show low shelf heating. Moreover, the technique is not affected by external magnetic fields. We have shown accurate primary thermometry down to 1 K and have proven that the low temperature range can be electrically tuned in-situ. For sub-10 mK operation, low transparency barriers and driving resonators with sub-200 MHz resonant frequencies should be used to ensure the thermometer is operated in the adiabatic limit and other materials such as GaAs could be used to improve the electron-phonon coupling.

When compared with other low-temperature primary electron thermometers, the GET presents some advantages and disadvantages. The GET requires a single tunnel barrier, similar to the SNT, but only a single reservoir. Both sensors must be probed by high-frequency techniques which provides an enhanced bandwidth over quasi-static measurements. However, the GET is unlikely to have the large dynamic range of the SNT since high temperature limit in the GET is set by quantum confinement. When compared to the CBT, which requires multiple tunnel barriers, the GET fabrication process is simpler with the trade-off that a low-temperature high-frequency amplification set-up is required but with the added benefit of the larger bandwidth. All three methods are independent of magnetic field as long as normal metals are used.

Overall, our thermometer shows potential for local probing of fast heat dynamics in nanoelectronic devices and it may have applications in the better study of thermal single-electron devices such as rectifiers and energy harvesters. Moreover, since the device is made using silicon technology it could naturally be integrated with silicon-based quantum circuits.

Methods

Device fabrication. The device used in this manuscript is fabricated on SOI substrate above the 145 nm buried oxide (BOX)[33]. The 8 nm thick NW channel channel is patterned using deep ultraviolet lithography (193 nm) followed by resist trimming process. For the gate stack, 1.9-nm HfSiON capped by 5 nm TiN and 50 nm polycrystalline silicon were deposited. The Si thickness under the HfSiON/TiN gate is 11 nm. After gate etching, a SiN layer (thickness 10 nm) was deposited and etched to form a first spacer on the sidewalls of the gate. 18-nm-thick Si raised source and drain contacts were selectively grown before the source/drain extension implantation and activation annealing. Then a second spacer was formed and followed by source/drain implantations, activation spike anneal and salicidation (NiPtSi).

Measurement set-up. Measurements are performed in an Oxford Instruments K400 dilution refrigerator with a base temperature of 40 mK. DC bias voltages (V_{sd}, V_{tg}, V_{bg}) are delivered through cryogenic constantant loom and discrete-component RC low-pass filters (cut-off frequency 10 kHz) at the mixing chamber. The source, drain and back gate lines are further filtered at the PCB with RC filters [$R = 10\,k\Omega$ 0603 thin film resistors TE-Connectivity RP73D1J10KBYDG and $C = 10$ nF 0603 NPO COG, KEMET, C0603C103J3GACTU]. The radio-frequency signal for gate-based readout is delivered through an attenuated and filtered coaxial line (Bandpass 250–500 MHz) which connects to a on-PCB bias tee. The gate voltage line has a 100 kΩ resistor in series (0603 thin film resistor, TE-Connectivity RP73D1J100KBTDG). The resonator consist of a 470 nH inductor, the sum of the samples parasitic capacitance to ground and the coupling capacitance C_c and the device which is couple to the resonator via the gate. The inductor is a surface mount wire-wound ceramic core (EPCOS B82498B series) and C_c is a high-Q 0.2 pF capacitor (Johanson Technology S-series EIA 0603), and the PCB is made from 0.8-mm-thick Rogers RO4003C laminate with an immersion silver finish. The reflected rf signal is amplified at 4 K (QuinStar QCAU350-30H) and room temperature, followed by quadrature demodulation (Polyphase Microwave AD0105B), from which the amplitude and phase of the reflected signal are obtained.

Data availability

The data that support the findings of this study are available from the corresponding author upon reasonable request.

Received: 10 May 2018 Accepted: 6 September 2018
Published online: 23 October 2018

References

1. Engert, J. et al. New evaluation of T-T_{2000} from 0.02 K to 1 K by independent thermodynamic methods. *Int. J. Thermophys.* **37**, 125 (2016).
2. White, D. R. Systematic errors in a high-accuracy Johnson noise thermometer. *Metrologia* **20**, 1 (1984).
3. Shibahara, A. et al. Primary current-sensing noise thermometry in the millikelvin regime. *Philos. Trans. A Math. Phys. Eng. Sci.* **374**, 20150054 (2016).
4. Spietz, L., Lehnert, K. W., Siddiqi, I. & Schoelkopf, R. J. Primary electronic thermometry using the shot noise of a tunnel junction. *Science* **300**, 1929–1932 (2003).
5. Spietz, L., Schoelkopf, R. J. & Pari, P. Shot noise thermometry down to 10 mK. *Appl. Phys. Lett.* **89**, 183123 (2006).
6. Iftikhar, Z. et al. Primary thermometry triad at 6 mK in mesoscopic circuits. *Nat. Commun.* **7**, 12908 (2016).
7. Pekola, J. P., Hirvi, K. P., Kauppinen, J. P. & Paalanen, M. A. Thermometry by arrays of tunnel junctions. *Phys. Rev. Lett.* **73**, 2903 (1994).
8. Bradley, D. I. et al. Nanoelectronic primary thermometry below 4 mK. *Nat. Commun.* **7**, 10455 (2016).
9. Hahtela, O. et al. Traceable Coulomb blockade thermometry. *Metrologia* **54**, 69 (2016).
10. Maradan, D. et al. GaAs quantum dot thermometry using direct transport and charge sensing. *J. Low Temp. Phys.* **175**, 784–798 (2014).
11. Mavalankar, A. et al. A non-invasive electron thermometer based on charge sensing of a quantum dot. *Appl. Phys. Lett.* **103**, 133116 (2013).
12. Gasparinetti, S., Martnez-Pérez, M. J., De Franceschi, S., Pekola, J. P. & Giazotto, F. Nongalvanic thermometry for ultracold two-dimensional electron domains. *Appl. Phys. Lett.* **100**, 253502 (2012).
13. Schmidt, D. R., Yung, C. S. & Cleland, A. N. Nanoscale radio-frequency thermometry. *Appl. Phys. Lett.* **83**, 1002–1004 (2003).
14. Rossi, A., Ferrus, T. & Williams, D. A. Electron temperature in electrically isolated Si double quantum dots. *Appl. Phys. Lett.* **100**, 133503 (2012).
15. Aradhya, S. V. & Venkataraman, L. Single-molecule junctions beyond electronic transport. *Nat. Nanotechnol.* **8**, 399 (2013).
16. Frake, J. C. et al. Radio-frequency capacitance spectroscopy of metallic nanoparticles. *Sci. Rep.* **5**, 10858 (2015).
17. Giazotto, F. & Martínez-Pérez, M. J. The Josephson heat interferometer. *Nature* **492**, 401 (2012).
18. Pekola, J. P. Towards quantum thermodynamics in electronic circuits. *Nat. Phys.* **11**, 118 (2015).
19. Partanen, M. et al. Quantum-limited heat conduction over macroscopic distances. *Nat. Phys.* **12**, 460 (2016).
20. Dutta, B. et al. Thermal conductance of a single-electron transistor. *Phys. Rev. Lett.* **119**, 077701 (2017).
21. Sivre, E. et al. Heat Coulomb blockade of one ballistic channel. *Nat. Phys.* **14**, 145 (2017).
22. Martínez-Pérez, M., Fornieri, A. & Giazotto, F. Rectification of electronic heat current by a hybrid thermal diode. *Nat. Nanotechnol.* **10**, 303 (2015).
23. Marcos-Vicioso, A., López-Jurado, C., Ruiz-Garcia, M. & Sánchez, R. Thermal rectification with interacting electronic channels: exploiting degeneracy, quantum superpositions and interference. *Phys. Rev. B* **98**, 035414 (2018).
24. Thierschmann, H. et al. Three-terminal energy harvester with coupled quantum dots. *Nat. Nanotechnol.* **10**, 854 (2015).
25. Vandersypen, L. M. K. et al. Interfacing spin qubits in quantum dots and donors-hot, dense, and coherent. *npj Quantum Info.* **3**, 34 (2017).
26. Veldhorst, M., Eenink, H. G. J., Yang, C. H. & Dzurak, A. S. Silicon CMOS architecture for a spin-based quantum computer. *Nat. Commun.* **8**, 1766 (2017).
27. Li, R. et al. A crossbar network for silicon quantum dot qubits. *Sci. Adv.* **4**, 3960 (2018).
28. Mizuta, R., Otxoa, R. M., Betz, A. C. & Gonzalez-Zalba, M. F. Quantum and tunneling capacitance in charge and spin qubits. *Phys. Rev. B* **95**, 045414 (2017).
29. Shevchenko, S. N. & Karpov, D. S. Thermometry and memcapacitance with a qubit-resonator system. *Phys. Rev. Appl.* **10**, 014013 (2018).
30. Cottet, A., Mora, C. & Kontos, T. Mesoscopic admittance of a double quantum dot. *Phys. Rev. B* **83**, 121311 (2011).
31. Colless, J. I. et al. Dispersive readout of a few-electron double quantum dot with fast rf gate sensors. *Phys. Rev. Lett.* **110**, 046805 (2013).
32. Gonzalez-Zalba, M. F., Barraud, S., Ferguson, A. J. & Betz, A. C. Probing the limits of gate-based charge sensing. *Nat. Commun.* **6**, 6084 (2015).
33. Betz, A. C. et al. High-frequency characterization of thermionic charge transport in silicon-on-insulator nanowire transistors. *Appl. Phys. Lett.* **104**, 043106 (2014).
34. Voisin, B. et al. Few-electron edge-state quantum dots in a silicon nanowire field-effect transistor. *Nano. Lett.* **14**, 2094–2098 (2014).
35. Chatterjee, A. et al. A silicon-based single-electron interferometer coupled to a fermionic sea. *Phys. Rev. B* **97**, 045405 (2018).
36. Harrison, P. & Valavanis, A. *Quantum wells, Wires and Dots,* (John Wiley and Sons, West Sussex, United Kingdom, 2016).

37. Persson, F., Wilson, C. M., Sandberg, M., Johansson, G. & Delsing, P. Excess dissipation in a single-electron box: the Sisyphus resistance. *Nano Lett.* **10**, 953–957 (2010).
38. Beenakker, C. W. J. Theory of Coulomb-blockade oscillations in the conductance of a quantum dot. *Phys. Rev. B* **44**, 1646 (1991).
39. Kouwenhoven, L. P. et al. Electron transport in quantum dots. *Proceedings of the NATO Advanced Study Institute on Mesoscopic Electron Transport* 105–214 (1997).
40. Chorley, S. J. et al. Measuring the complex admittance of a carbon nanotube double quantum dot. *Phys. Rev. Lett.* **108**, 036802 (2012).
41. Gonzalez-Zalba, M. F. et al. Gate-sensing coherent charge oscillations in a silicon field-effect transistor. *Nano Lett.* **16**, 1614–1619 (2016).
42. Betz, A. C. et al. Dispersively detected Pauli spin-blockade in a silicon nanowire field-effect transistor. *Nano Lett.* **15**, 4622–4627 (2015).
43. Ahmed, I. et al. Radio-frequency capacitive gate-based sensing. *Phys. Rev. Appl.* **10**, 014018 (2018).

Acknowledgements

We thank Jonathan Prance for providing useful comments. This research has received funding from the European Union's Horizon 2020 Research and Innovation Programme under grant agreement No 688539 (http://mos-quito.eu), No 732894 (FET Proactive HOT) and the Winton Programme of the Physics of Sustainability. I.A. is supported by the Cambridge Trust and the Islamic Development Bank. A.C. acknowledges support from the EPSRC Doctoral Prize Fellowship.

Author contributions

M.F.G.Z. devised the experiment. I.A., A.C., and M.F.G.Z. performed the experiment. S.B. fabricated the sample. I.A., J.A.H., J.J.L.M., and M.F.G.Z. analyzed the data. All authors contributed in the writing of the manuscript.

Additional information

Supplementary Information accompanies this paper at https://doi.org/10.1038/s42005-018-0066-8.

Competing interests: The authors declare no competing interests.

Reprints and permission information is available online at http://npg.nature.com/reprintsandpermissions/

Publisher's note: Springer Nature remains neutral with regard to jurisdictional claims in published maps and institutional affiliations.

Open Access This article is licensed under a Creative Commons Attribution 4.0 International License, which permits use, sharing, adaptation, distribution and reproduction in any medium or format, as long as you give appropriate credit to the original author(s) and the source, provide a link to the Creative Commons license, and indicate if changes were made. The images or other third party material in this article are included in the article's Creative Commons license, unless indicated otherwise in a credit line to the material. If material is not included in the article's Creative Commons license and your intended use is not permitted by statutory regulation or exceeds the permitted use, you will need to obtain permission directly from the copyright holder. To view a copy of this license, visit http://creativecommons.org/licenses/by/4.0/.

© The Author(s) 2018